EES Catalysis

PAPER

View Article Online
View Journal | View Issue

Check for updates

Cite this: *EES Catal.*, 2026, 4, 189

Active Pt thin layers over MoC for the low-temperature water–gas shift reaction

Peiyao Guo,†[ac] Yinghong Huang,†[b] Chuanchuan Jin,[a] Di Zhou,[a] Shaobo Han,[a] Yan Zhou,*[a] Fan Yang[b] and Wenjie Shen*[ab]

Received 10th August 2025,
Accepted 9th September 2025

DOI: 10.1039/d5ey00243e

rsc.li/eescatalysis

Pt/MoC catalysts have been documented to be highly active for the water–gas shift reaction at low temperatures, but identification of the active metal entity remains challenging primarily because of the co-existence of metal nanoparticles, clusters and single-atoms in the catalysts. Here, Pt dispersion on MoC was finely tuned by the carburization of a Pt/MoO_3 precursor with a CH_4/H_2 mixture at 873–973 K. It was found that the 3 nm Pt particles over MoO_3 redispersed into thin layers (mainly bilayers/trilayers) at 873 K and into loosely arranged monolayers/single-atoms at 973 K during the carburization of MoO_3 to MoC. Tests for the low-temperature water–gas shift reaction found that Pt thin layers showed the most pronounced activity based on the moderate adsorption of CO on Pt and the facile dissociation of water over MoC at their interfacial perimeter. But the activity lowered as Pt further dispersed into monolayers/single-atoms in the Pt/MoC catalysts. *In situ* IR experiments revealed that the Pt thin layers facilitated the adsorption of CO while the MoC support dissociated H_2O into reactive –OH species that might migrate to the Pt surface and react with CO, expediting the low-temperature WGS reaction.

Broader context

Pt/MoC catalysts are highly active for the low-temperature water–gas shift (WGS) reaction, a crucial step in energy catalysis related to the syngas industry to adjust the proportions of CO and H_2 in the feed streams for chemical synthesis and to produce hydrogen for the proton exchange membrane fuel cells. A straightforward identification of the intrinsic active Pt entity is challenging because of the co-existence of nanoparticles, clusters and single-atoms over the MoC support. This work finely tuned Pt dispersion during the preparation of Pt/MoC catalysts *via* carburization of a Pt/MoO_3 precursor with a CH_4/H_2 mixture at 873–973 K. The topological transition of MoO_3 to α-MoC drove the dispersion of 3 nm Pt particles into bi/trilayers at 873 K while into monolayers/single-atoms at 973 K. Catalytic tests for the low-temperature WGS reaction found that the activity increased initially by downsizing the Pt particles to bi/trilayers but then declined as the Pt thin layers further disintegrated into monolayers/single-atoms. This finding experimentally demonstrated that Pt bi/trilayers acted as the most active entity for the WGS reaction that occurred at the Pt–MoC interface and fundamentally elaborated the atomic structure of the active Pt species.

Introduction

The low-temperature water–gas shift (WGS) reaction, converting H_2O/CO to H_2/CO_2, is a crucial step in the production of syngas and/or H_2 by steam reforming of hydrocarbons/oxygenates.[1] It adjusts the proportions of CO and H_2 in the reformate for downstream applications such as ammonia synthesis, methanol synthesis, and Fischer–Tropsch synthesis. This reaction has also been applied to produce H_2 for the proton exchange membrane fuel cells, which require as little residual CO in the hydrogen stream as possible for preventing the fuel cell catalyst from poisoning.[1,2] The WGS reaction is thermodynamically favorable at low-temperatures, but it proceeds rather slowly over the conventional Cu-based catalysts.[1–3] Noble-metals, supported by transition-metal carbides, have been reported to catalyze efficiently the low-temperature WGS reaction.[4–12] For example, Pt/MoC and Au/MoC are highly active for the WGS reaction in the temperature range 373–423 K.[4,5,7,9,12] Mechanistic and kinetic studies suggested that the reaction occurred at the metal–support interface, where the size of noble-metal and the crystalline structure of carbide played decisive roles.[7,9–14] The noble-metal adsorbed CO while the MoC support dissociated H_2O, and the high activity was ascribed to the superior ability of MoC to dissociate H_2O.[7–10,15–18] It was also proposed that the enhanced WGS activity could be ascribed to electronic

[a] *State Key Laboratory of Catalysis, Dalian Institute of Chemical Physics, Chinese Academy of Sciences, Dalian, 116023, China. E-mail: zhouyan@dicp.ac.cn, shen98@dicp.ac.cn*
[b] *School of Physical Science and Technology, ShanghaiTech University, Shanghai, 201210, China*
[c] *University of Chinese Academy of Sciences, Beijing, 100049, China*
† These authors contributed equally to this work.

Open Access Article. Published on 15 September 2025. Downloaded on 2/8/2026 1:21:08 AM. This article is licensed under a Creative Commons Attribution 3.0 Unported Licence.

Open Access Article. Published on 15 September 2025. Downloaded on 2/8/2026 1:21:08 AM. This article is licensed under a Creative Commons Attribution 3.0 Unported Licence.

perturbations in the noble-metal particles caused by MoC, affecting the adsorption of CO.[4] Therefore, tuning the geometric and electronic structure of the noble-metal–carbide interface, regarding the surface property of the molybdenum carbide and the dispersion of the noble-metal entity, constitutes a practical strategy to promote the WGS activity at low temperatures.

MoC has similar electronic characteristics to those of noble-metals below the Fermi level and thereby bonds with noble-metals favorably.[19] Depending on the loading amount, noble-metals may be present as nanoparticles, clusters, and single-atoms in the catalysts and thus form different interfacial configurations. In this sense, identifying the active metal entity remains challenging, especially for atomic clusters and single-atoms. For example, by increasing the loading amount of Pt, single-atoms, clusters, and particles were formed over α-MoC.[9] Pt single-atoms were obtained when the metal loading was below 0.2 wt%, while Pt clusters emerged at 2.0 wt%. This dispersion of Pt affected the WGS activity and stability significantly. The specific activity of Pt single-atoms (2.18 mol_{H_2} mol_{Pt}^{-1} s^{-1}) at 393 K was much greater than that of Pt clusters (0.74 mol_{H_2} mol_{Pt}^{-1} s^{-1}). However, the single-atoms deactivated rapidly, because of the oxidation of α-MoC under the reaction conditions, but the clusters remained relatively stable due to the crowding surface Pt sites that prevented the α-MoC surface from oxidation by water.[9,18] By contrast, Pt clusters have been reported to be more active than Pt single-atoms. The specific activity of fully exposed Pt monolayers on α-MoC_{1-x} was one order of magnitude greater than that of Pt single-atoms for the WGS reaction at 373–473 K.[20] A linear correlation between the WGS activity and the size of the Pt monolayer revealed that the interfacial perimeter served as the active site for the WGS reaction. The crucial role of the Pt–MoC interface in promoting WGS performance has been verified by varying the size of raft-like Pt particles over Mo_2C.[13] As the Pt loading amount is increased (0.5–12.0 wt%), raft-like Pt particles over Mo_2C enlarged in size, but the geometry remained at 1–2 atomic layers because of the strong Pt–Mo_2C interfacial bonding. The specific reaction rate lowered from 5.2 to 0.7 mol_{H_2} mol_{Pt}^{-1} s^{-1} at 513 K, suggesting that the reaction occurred at the interfacial perimeter. It was further speculated that CO adsorbed on Pt sites and subsequently reacted with hydroxyl species generated by H_2O dissociation at Mo_2C.

To date, identifying the active Pt entity on molybdenum carbides for the low-temperature WGS reaction remains a subject of debate, primarily because of the difficulty in precisely controlling Pt dispersion over MoC. In a previous study, we have reported that Au particles could undergo redispersion into atomic layers and isolated atoms during MoO_3 carburization to α-MoC with a CH_4/H_2 mixture at 873–1023 K. The WGS activity at 393 K showed a volcano-type pattern with respect to the coordination number of Au–Au in the size-specified gold entities, and Au atomic layers having an Au–Au coordination number of 7.7 were intrinsically more active.[11] In this work, we extended the study to examine the redispersion of Pt nanoparticles during MoO_3 carburization to α-MoC and quantify the activities of Pt particles, thin layers, and single-atoms for the low-temperature WGS reaction. It was found that Pt bi/trilayers were intrinsically more active than Pt monolayers/single-atoms on α-MoC at the same metal loading amount (0.56 wt%). The Pt thin layers facilitated the adsorption of CO while the MoC support dissociated H_2O at their interfaces, and the resulting –OH species might migrate to the Pt surface and react with CO, promoting the WGS activity.

Methods

Catalyst preparation

MoO_3 nanobelts were prepared using a hydrothermal method, as we previously described.[21,22] Pt particles, with a mean size of 2.7 nm (Fig. S1, SI), were synthesized by the reduction of H_2PtCl_6 in a methanol/water mixture using PVP (M_w = 10 000) as the capping agent.[23] 0.135 g of PVP, 180 mL of methanol, 14 mL of H_2O and 6.5 mL of 19.3 mmol L^{-1} H_2PtCl_6 aqueous solution were mixed, heated to 338 K, and refluxed at that temperature for 3 h. After cooling down to room temperature, the solid product was collected by centrifugation and washed with ethanol and H_2O. The Pt particles were then dispersed in 50 mL of H_2O, yielding a colloidal solution with a Pt concentration of 0.49 mg_{Pt} mL^{-1}.

The Pt/MoO_3 sample was prepared by dispersing the Pt particles onto the MoO_3 nanobelts using a colloid-deposition method. 0.3 g MoO_3 nanobelts were dispersed in 10 mL of H_2O and subjected to ultrasound treatment for 30 minutes. Then, 100 mL of acetic acid was added, followed by the addition of 3.1 mL of Pt colloids (0.49 mg_{Pt} mL^{-1} in H_2O). The suspension was stirred at room temperature for 5 h. The solid was collected by centrifugation, dried at 353 K for 12 h and finally calcined at 673 K in air for 4 h. The loading amount of Pt in the Pt/MoO_3 sample was 0.56 wt%, measured by inductively coupled plasma optical emission spectrometry (ICP-OES) using an ICP-OES 7300DV instrument.

The Pt/α-MoC catalysts were then obtained by treating the Pt/MoO_3 sample with a 20 vol% CH_4/H_2 mixture at 873–973 K. Specifically, the Pt/MoO_3 sample was loaded into a fixed-bed quartz tubular reactor, heated from room temperature to 573 K at a rate of 5 K min^{-1} and then to 873 or 973 K at a rate of 1 K min^{-1} under the flow of a 20 vol% CH_4/H_2 mixture (15 mL min^{-1}), and held at 873 or 973 K for a certain period (up to 16 h). The catalyst, thus obtained, was labeled as Pt-*T*-*x*, where *T* stands for the temperature and *x* refers to the time of carburization. For structure characterization, the sample was cooled down to room temperature naturally and passivated by flowing a 1 vol% O_2/N_2 mixture (30 mL min^{-1}) for 4 h before exposure to air.

Catalyst characterization

The X-ray powder diffraction (XRD) pattern was recorded using a D/Max-2500/PC diffractometer (Rigaku) operated at 40 kV and 200 mA with a Cu K_α radiation source.

© 2026 The Author(s). Published by the Royal Society of Chemistry

Open Access Article. Published on 15 September 2025. Downloaded on 2/8/2026 1:21:08 AM. This article is licensed under a Creative Commons Attribution 3.0 Unported Licence.

Transmission electron microscopy (TEM) images were taken using a Hitachi HT7700 microscope at 120 kV. Aberration-corrected scanning TEM (STEM) images and energy dispersive X-ray spectroscopy (EDS) elemental mappings were acquired over a JEM-ARM300F microscope at 300 kV. The specimen was prepared by ultrasonically dispersing the powder sample into ethanol, depositing droplets of the suspension onto lacey carbon-coated copper grids, and drying in air.

X-ray photoelectron spectra (XPS) were acquired over a Thermo Fisher ESCALAB 250Xi spectrometer using an Al K_α radiation source. The Pt/MoO_3 sample was carburized in a continuous-flow fixed-bed quartz tubular reactor and subsequently transferred into a glove box, where it was mounted on an airtight XPS sample holder. The sealed sample holder was then transferred to the XPS chamber, where the spectra of Pt 4f, Mo 3d, O 1s and C 1s were recorded. The charging effect was corrected by calibrating the binding energy of C 1s in molybdenum carbide to 283.2 eV.

Infrared (IR) spectra of CO and H_2O adsorptions on Pt/α-MoC catalysts were recorded on an ultrahigh vacuum (UHV) apparatus, combining an IR spectrometer (Bruker VERTEX 80v) with a homemade *in situ* IR cell.[24] The passivated Pt/α-MoC sample was first reactivated with a 20 vol% CH_4/H_2 mixture (30 mL min^{-1}) at 863 K for 2 h. After cooling down to room temperature under an N_2 flow, the sample was transferred promptly to the IR cell, where it was further treated with H_2 (1 mbar) at 863 K for 30 min. The sample was then exposed to CO or H_2O (10 mbar) for 30 min at room temperature (303 K) and heated gradually to 473 K. The IR spectra were recorded after evacuation (1.0×10^{-5} mbar) at the desired temperature with 128 scans at 4 cm^{-1} resolution. Each spectrum was referenced to a background spectrum obtained before gas introduction.

Catalytic test

The WGS reaction on the Pt/MoC catalysts was performed using a continuous-flow fixed-bed quartz tubular reactor (6 mm, inner diameter) at atmospheric pressure. 80 mg of Pt/MoO_3 was placed between two layers of quartz wools inside the reactor and was carburized with a 20 vol% CH_4/H_2 mixture (15 mL min^{-1}) at 873 or 973 K for a certain period. After cooling down to 393 K under a He flow, the catalyst was exposed to a 3.0 vol% CO/6.0 vol% H_2O/He mixture (66.7 mL min^{-1}), and the reaction was tested for about 9 hours. The effluent from the reactor was analyzed online using a gas chromatograph equipped with a thermal conductivity detector and a flame ionization detector.

For the kinetic study, the reaction tests were performed under a differential reactor condition by controlling the conversion of CO below 15%. The specific reaction rates were calculated on the mass of Pt in the catalyst, *i.e.*, moles of CO converted per mole Pt per second (mol_{CO} mol_{Pt}^{-1} s^{-1}). The turnover frequency (TOF) of the interfacial Pt site was estimated based on the models of Pt bilayers, monolayers and single-atoms.

Results and discussion

Redispersion of Pt particles to thin layers

The XRD pattern of the Pt/MoO_3 sample confirmed that the MoO_3 support had an orthorhombic structure (Fig. 1a). The {020} diffraction line at 12.8° and the {040} diffraction line at 25.7° intensified significantly, indicating a preferential exposure of the {010} facets. STEM images showed the uniform distribution of Pt particles on MoO_3 nanobelts, with an average size of 2.9 nm in the range of 1.5–4.8 nm (Fig. 1b–f). The lattice spacing of 0.20 nm was ascribed to MoO_3 (200) facets (Fig. 1c)

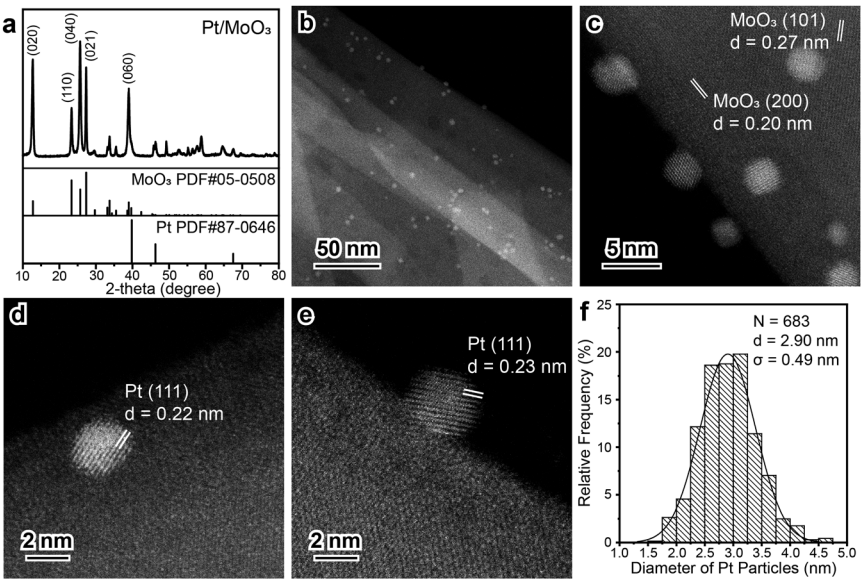

Fig. 1 Structure of the Pt/MoO_3 sample. (a) XRD pattern, (b)–(e) STEM images, and (f) size distribution of Pt particles.

Open Access Article. Published on 15 September 2025. Downloaded on 2/8/2026 1:21:08 AM.
This article is licensed under a Creative Commons Attribution 3.0 Unported Licence.

while the lattice spacing of 0.22/0.23 nm referred to Pt (111) on the spherical Pt particles (Fig. 1d and e).

The Pt/MoO_3 sample was then carburized with a CH_4/H_2 mixture at 873 K for up to 16 hours. XRD patterns recorded at different intervals evidenced the gradual transformation of MoO_3 to α-MoC (Fig. 2 and Table S1, SI). Upon heating the Pt/MoO_3 sample to 873 K (Pt-873-0), MoO_3 was converted into MoO_xC_y with a cell parameter of 0.413 nm.[25] At 2 h (Pt-873-2), the cell parameter increased to 0.421 nm, corresponding to crystalline α-MoC. This cell expansion was caused by the insertion of carbon atoms into the octahedral or cubic prism voids of Mo through formation of Mo–C bonds, leading to the shrinkage of the metal d-band and the increase of the density of states below the Fermi level in molybdenum carbides.[19] As the carburization extended to 4–16 h, the cell parameter stabilized at 0.421 nm, indicating that the carbon content in the carbides remained basically unchanged.[26] The diffraction lines, especially {111} and {200} of α-MoC, shifted gradually towards smaller angles over time, signifying the progressive incorporation of C atoms into the lattice, causing expansion of the unit cell. The surface properties of the Pt-873-0, Pt-873-2 and Pt-873-6 samples were analyzed using XPS (Fig. 3). The binding energy of Pt $4f_{7/2}$ for Pt-873-0 was located at 71.5 eV, indicative of metallic Pt over MoC.[20,27–30] As the carburization time extended to 2 and 6 h, the binding energy of Pt $4f_{7/2}$ remained nearly unchanged, at 71.7–71.8 eV. These binding energies were slightly higher than those for Pt nanoparticles, implicating electron transfer from Pt to MoC in the Pt/α-MoC catalysts as commonly observed.[20,29–31] The binding energies for Mo $3d_{5/2}$ appeared at 228.3 eV (Mo^{2+}), 229.0 eV (Mo^{3+}), and 231.3 eV (Mo^{4+}) with Mo^{2+} being the dominant.[11,25,32] The Mo^{2+} content increased from 23.0% in Pt-873-0 to 46.8% in Pt-873-2 and 53.9% in Pt-873-6, indicating the enhanced carburization. The binding energy of C 1s at 283.2 eV corresponded to the carbide carbon.[32] The surface carbide C/Mo ratio increased rapidly from 0.28 in Pt-873-0 to 0.42 in Pt-873-2 and further to 0.45 in Pt-873-6, evidencing the gradual incorporation of C atoms into the lattice with extended carburization time. The binding energies of O 1s at 530.2 and 531.3 eV referred to the lattice oxygen (O_L) and the adsorbed hydroxyl, respectively, on the MoC surface.[11,22,33,34] The surface O_L/Mo ratio decreased pronouncedly from 0.45 in Pt-873-0 to 0.34 in Pt-873-2 and 0.33 in Pt-873-6 as the carburization was enhanced. Altogether, the transition of molybdenum oxycarbide to molybdenum carbide occurred significantly at the early 2 hours at 873 K.

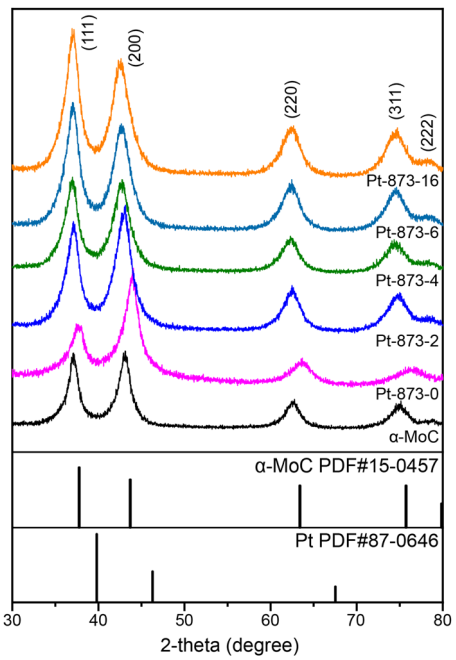

Fig. 2 XRD patterns of the Pt-873-*x* samples.

STEM images identified the redispersion of Pt particles during the carburization of MoO_3 to α-MoC at 873 K. In the Pt-873-0 sample, Pt particles had a hemispherical morphology with an average size of 3.3 nm, exposing the (200) facets indexed by the lattice spacing of 0.19 nm (Fig. 4a–c and Fig. S2, SI). EDS elemental mappings evidenced the uniform distribution of Pt particles (Fig. 4d). For the Pt-873-2 sample, hemispherical Pt particles and thin layers were observed on α-MoC (Fig. 4e–l and Fig. S3, SI). Pt species mainly exposed (220) facets during the redispersion process as determined by the FFT pattern (Fig. 4f). The number of Pt particles reduced significantly, while that of Pt thin layers enhanced dramatically. Line-scanning intensity profiles revealed that the Pt thin layers were about 3 atomic layers thick (Fig. 4i–l). In the Pt-873-6 sample, Pt particles nearly disappeared while mainly Pt thin layers dispersed on α-MoC. They were 1–3 nm in width while 2–3 atomic layers in thick (Fig. 5a–h and Fig. S4, SI) and mainly exposed (200) facets (Fig. 5b). EDS elemental mappings also evidenced that Pt nanoparticles disappeared while Pt thin layers dominated, suggesting that Pt dispersion gradually improved with increasing the carbonization time from 0 to 6 hours. When extending the carburization to 16 h, Pt thin layers still presented as the main entities (Fig. S5, SI). Therefore, it could be inferred that the initial Pt particles underwent redispersion, induced by the transformation of MoO_xC_y to α-MoC, split and diffused on the α-MoC surface, and ultimately stabilized as Pt bi/trilayers (Fig. 5i).

Redispersion of Pt thin layers to monolayers/single-atoms

To enhance Pt redispersion, the Pt/MoO_3 sample was subjected to carburization in a CH_4/H_2 mixture at a higher temperature, 973 K. The XRD pattern of the Pt-973-0 sample evidenced α-MoC in the fcc phase with a cell parameter of 0.421 nm (Fig. 6 and Table S1, SI). This result illustrated that carburization at 973 K accelerated the topological transformation of MoO_3 to α-MoC. Upon extending the carburization to 6–10 h, the cell parameter of α-MoC remained at 0.422 nm, accompanied by minor shifts of the {111} and {200} diffraction lines to lower angles, meaning a slight increase in carbon content in the carbide.[26] The increasing intensity of the α-MoC {200} diffraction suggests the enhanced crystallinity.

XPS analysis revealed the surface composition of the Pt-973-0 and Pt-973-6 samples (Fig. 7). The binding energy of Pt $4f_{7/2}$ is

© 2026 The Author(s). Published by the Royal Society of Chemistry

Open Access Article. Published on 15 September 2025. Downloaded on 2/8/2026 1:21:08 AM.
This article is licensed under a Creative Commons Attribution 3.0 Unported Licence.

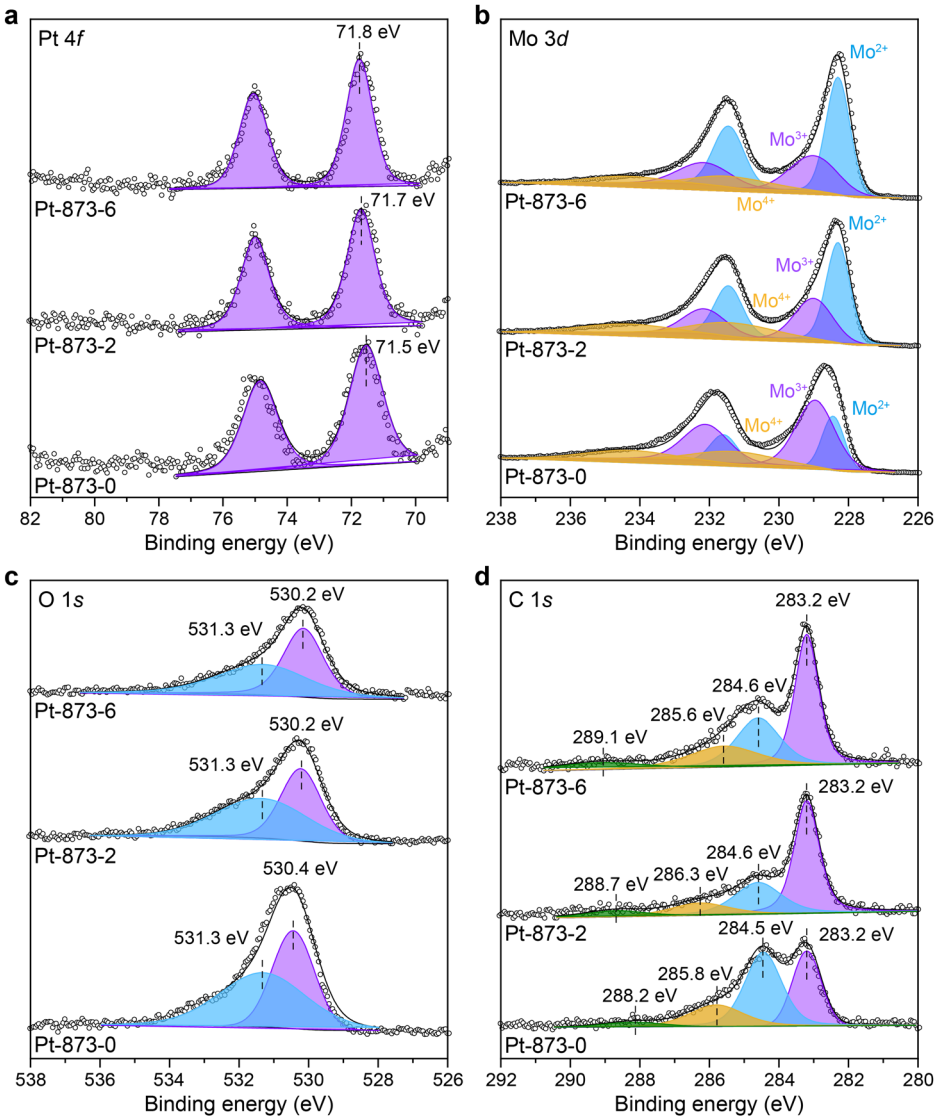

Fig. 3 XPS spectra of the Pt-873-*x* samples. (a) Pt 4f, (b) Mo 3d, (c) O 1s, (d) C 1s.

located at 71.8 eV, indicating metallic Pt but with charge transfer to MoC.[20,29–31] The binding energies for Mo $3d_{5/2}$ included 228.3 eV (Mo^{2+}), 229.0 eV (Mo^{3+}), and 231.3 eV (Mo^{4+}), where Mo^{2+} is dominant.[11,25,32] The surface carbide C/Mo ratio increased from 0.43 in Pt-973-0 to 0.49 in Pt-973-6, evidencing the incorporation of C atoms into the lattice. The binding energy of O 1s at 530.2 eV corresponded to the lattice oxygen on the MoC surface,[11,22,33,34] while the surface O_L/Mo ratio lowered from 0.36 in Pt-973-0 to 0.32 in Pt-973-6 due to the carburization over time.

STEM and IR analyses verified the structure evolution of Pt particles during the carburization at 973 K. For the Pt-973-0 sample, Pt thin layers were observed on α-MoC, along with a few single-atoms (Fig. 8a–f and Fig. S6, SI). Line-scanning intensity profiles, relative to that of Pt single-atoms, revealed that the Pt thin layers were 2–3 atoms thick, *i.e.*, bilayers and trilayers. The Pt single-atoms predominantly resided on the well-crystallized α-MoC surface near the Pt bi/trilayers. The CO-IR spectrum showed distinct bonds for CO adsorption over both Pt and MoC (Fig. 9a). The band at 2130 cm^{-1} referred to CO linearly bound to $Pt^{\delta+}$ single-atoms while the signal at 2078 cm^{-1} indicated CO adsorbed on Pt bi/trilayers.[35–39] Meanwhile, the bands at 2122 and 2164 cm^{-1}, with a shoulder at 2200 cm^{-1}, were ascribed to CO adsorbed on molybdenum carbides.[6,40,41] As the temperature was increased to 473 K, the intensity of CO adsorbed on molybdenum carbide decreased moderately, while the intensity of CO adsorbed on the Pt bi/trilayers remained essentially unchanged, suggesting a stronger adsorption of CO. In the Pt-973-6 sample, Pt monolayers became dominant, accompanied by a substantial number of Pt single-atoms (Fig. 8g–l and Fig. S7, SI). This was reaffirmed by EDS elemental mappings, where atomically dispersed Pt could be clearly seen (Fig. S7d, SI). For the Pt-973-10 sample, Pt single-atoms dominated, together with a few loosely arranged monolayers that could be viewed approximately as single-atoms (Fig. 8m–o and Fig. S8, SI). The CO-IR spectrum

© 2026 The Author(s). Published by the Royal Society of Chemistry

Open Access Article. Published on 15 September 2025. Downloaded on 2/8/2026 1:21:08 AM.
This article is licensed under a Creative Commons Attribution 3.0 Unported Licence.

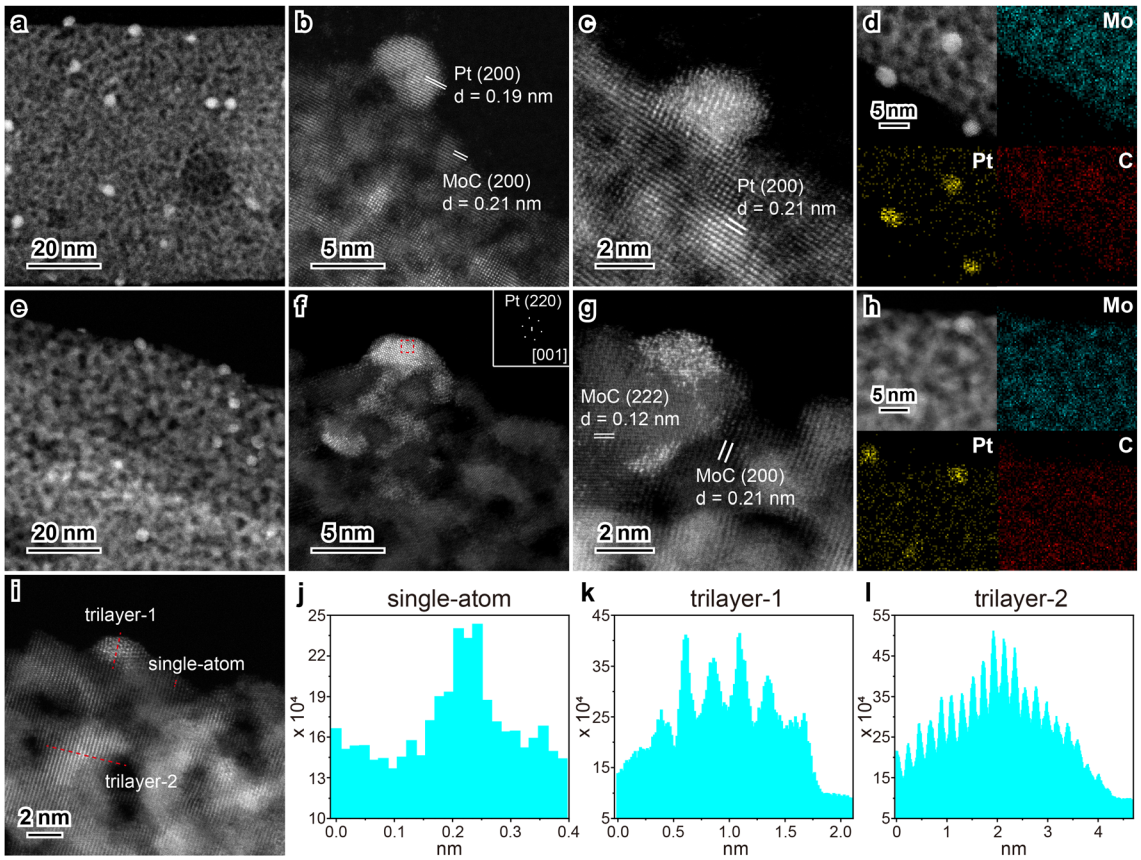

Fig. 4 Geometric structures of the Pt-873-0 (a)–(d) and Pt-873-2 (e)–(l) samples. The inset in f is the FFT pattern corresponding to the red rectangular box. Pt thin layers are identified by comparing their line-scanning intensity profiles (i)–(l) to that of a Pt single-atom.

further evidenced the presence of atomically dispersed Pt sites (Fig. 9b). The band at 2130 cm^{-1} indicated CO linearly adsorbed over $Pt^{\delta+}$ single-atoms, while the signals at 2086 and 2063 cm^{-1} referred to linear adsorbed CO on Pt monolayers.[36,37,39,42–44] Again, the prominent bands at 2121 and 2163 cm^{-1} and the shoulder peak at 2212 cm^{-1} could be assigned to CO adsorbed on MoC.[6,40,41] As the temperature was raised to 473 K, CO adsorbed on molybdenum carbide weakened, whereas that adsorbed on Pt single-atoms remained unchanged. These STEM and IR data highlighted collectively that carburization of the Pt/MoO_3 sample at 973 K promoted the dispersion of Pt thin layers further to single-atoms/monolayers over α-MoC (Fig. 8p). This observation is consistent with our previous study on the redispersion of Au particles on α-MoC, where the temperature for carburization was the primary driving force for the redispersion of the metal particles over α-MoC.[12]

Low-temperature WGS reaction over the Pt/MoC catalysts

The Pt/MoC catalysts were evaluated for the WGS reaction at 393 K to quantify the activities of Pt particles, thin layers, and monolayers/single-atoms. The conversion of CO was about 4% on Pt-873-0, increased sharply to 19% over Pt-873-2 and further to 26% on the Pt-873-6 catalyst (Fig. 10a). Correspondingly, the specific reaction rate increased from 0.032 mol_{CO} mol_{Pt}^{-1} s^{-1} of Pt-873-0 to 0.141 mol_{CO} mol_{Pt}^{-1} s^{-1} of Pt-873-2 and further to 0.160 mol_{CO} mol_{Pt}^{-1} s^{-1} of Pt-873-6 (Table S2, SI). This increasing activity was well correlated with the redispersion of Pt from particles to thin layers. The lower activity of Pt-873-0 was linked to the large Pt particles (3.3 nm) and the insufficient carburization of MoO_3, existing predominantly in the form of MoO_xC_y, which was weak for water dissociation. For the Pt-873-2 catalyst, the increasing proportion of Pt thin layers extended the Pt–MoC interface that contributed to the improved WGS activity. In the Pt-873-6 catalyst, Pt mainly existed as bilayers and trilayers that enlarged the Pt–MoC interface considerably and thus exhibited a superior WGS activity. Of note, the WGS activity on Pt-873-16 was comparable to that of Pt-873-6, suggesting that the dispersion of Pt and the surface structure of molybdenum carbide remained essentially unchanged, as verified by the XRD and STEM data (Fig. S9, SI). XPS spectra of the spent catalysts, tested for 2 hours under the reaction conditions, revealed that Pt entities basically remained at the metallic state with Pt $4f_{7/2}$ binding energies of 71.6–71.7 eV (Fig. S10, SI), implicating that water had a negligible effect on Pt. However, the MoC support was partially oxidized by water during the reaction. For the Pt-873-0 sample, the fraction of surface Mo^{2+} lowered from 23.0% over the fresh catalyst to 16.2% on the spent one, suggesting that the MoO_xC_y support was susceptible to oxidation by H_2O. By contrast, the

© 2026 The Author(s). Published by the Royal Society of Chemistry

Open Access Article. Published on 15 September 2025. Downloaded on 2/8/2026 1:21:08 AM. This article is licensed under a Creative Commons Attribution 3.0 Unported Licence.

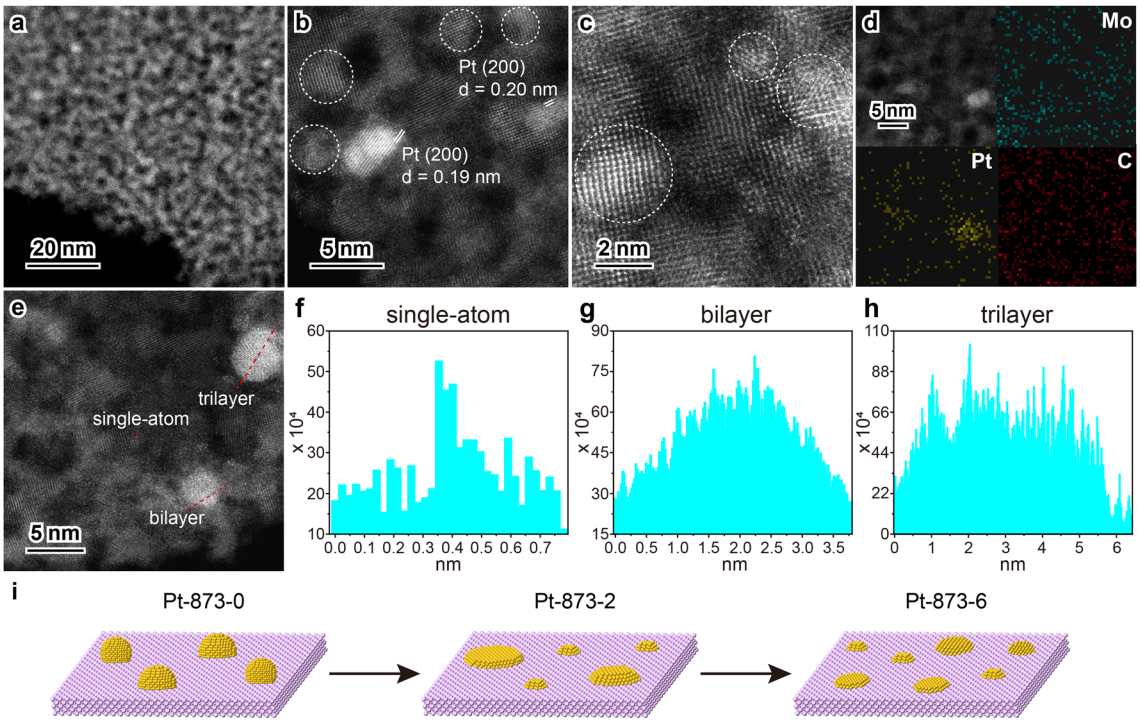

Fig. 5 Geometric structure of the Pt-873-6 sample. (a)–(c) STEM images. The circles indicate Pt thin layers. (d) EDS elemental mappings. (e)–(h) Line-scanning intensity profiles of a Pt single-atom, bilayer and trilayer. Pt thin layers are identified by comparing their line-scanning intensity profiles to that of a Pt single-atom. (i) A schematic illustration of redispersion of Pt particles to thin layers.

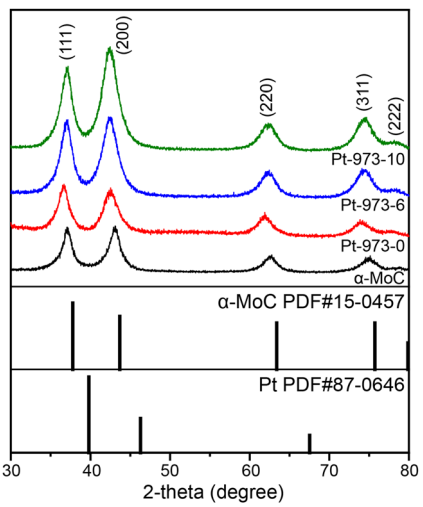

Fig. 6 XRD patterns of the Pt-973-*x* samples.

fraction of surface Mo^{2+} changed marginally before and after the reaction (53.9–54.9%) over the Pt-873-6 catalyst. Regarding surface oxygen species, the OH/O_L ratio remained consistent before and after the reaction (1.25–1.33) on the Pt-873-0 catalyst, suggestive of the limited ability of the MoO_xC_y support to dissociate water. But this ratio increased from 1.03 in the fresh Pt-873-6 sharply to 2.52 over the spent one, evidencing the superior ability of the MoC support for the dissociation of water molecules.

Interestingly, the WGS activity declined when the Pt dispersion in the Pt-973-*x* catalysts was enhanced. The conversion of CO was 24% over Pt-973-0, lowered to 16% over Pt-973-6 and 12% over Pt-973-10 (Fig. 10b). The specific reaction rate decreased rapidly from 0.153 mol_{CO} mol_{Pt}^{-1} s^{-1} for Pt-973-0 to 0.087 mol_{CO} mol_{Pt}^{-1} s^{-1} for Pt-973-6 and further lowered to 0.078 mol_{CO} mol_{Pt}^{-1} s^{-1} for Pt-973-10 (Table S2, SI). This decrease in activity could be ascribed to the evolution of Pt structure, *i.e.*, Pt redispersion from thin layers to monolayers/single-atoms. In the Pt-973-0 catalyst, Pt mostly existed as bilayers and trilayers, similar to the case of Pt-873-6. The Pt-973-6 sample consisted of Pt monolayers/single-atoms, while Pt single-atoms dominated in the Pt-973-10 sample. The turnover frequency (TOF) of the interfacial Pt site was estimated based on the models of Pt bilayer, monolayer and single-atom (Fig. 8). It was 2.75 s^{-1} for Pt-973-0, 0.70 s^{-1} for Pt-973-6, and 0.08 s^{-1} for Pt-973-10, evidencing that Pt bilayers were intrinsically more active for the WGS reaction. These reaction data agreed with previous reports that Pt single-atoms showed much lower activity in both low-temperature WGS reaction and CO oxidation, partly because of the strong binding of CO on Pt.[36] Strong adsorption of CO on Pt inhibited its interaction with water, thereby reducing the WGS activity. In this sense, the Pt-873-6 and Pt-973-0 catalysts with Pt dispersion at Pt bilayers and trilayers showed comparable or even better performance for the WGS reaction at low-temperatures, for example, 393 K, than most MoC-supported noble-metal catalysts under identical or close reaction conditions (Table S2, SI). Moreover, the Pt-973-0

Open Access Article. Published on 15 September 2025. Downloaded on 2/8/2026 1:21:08 AM.
This article is licensed under a Creative Commons Attribution 3.0 Unported Licence.

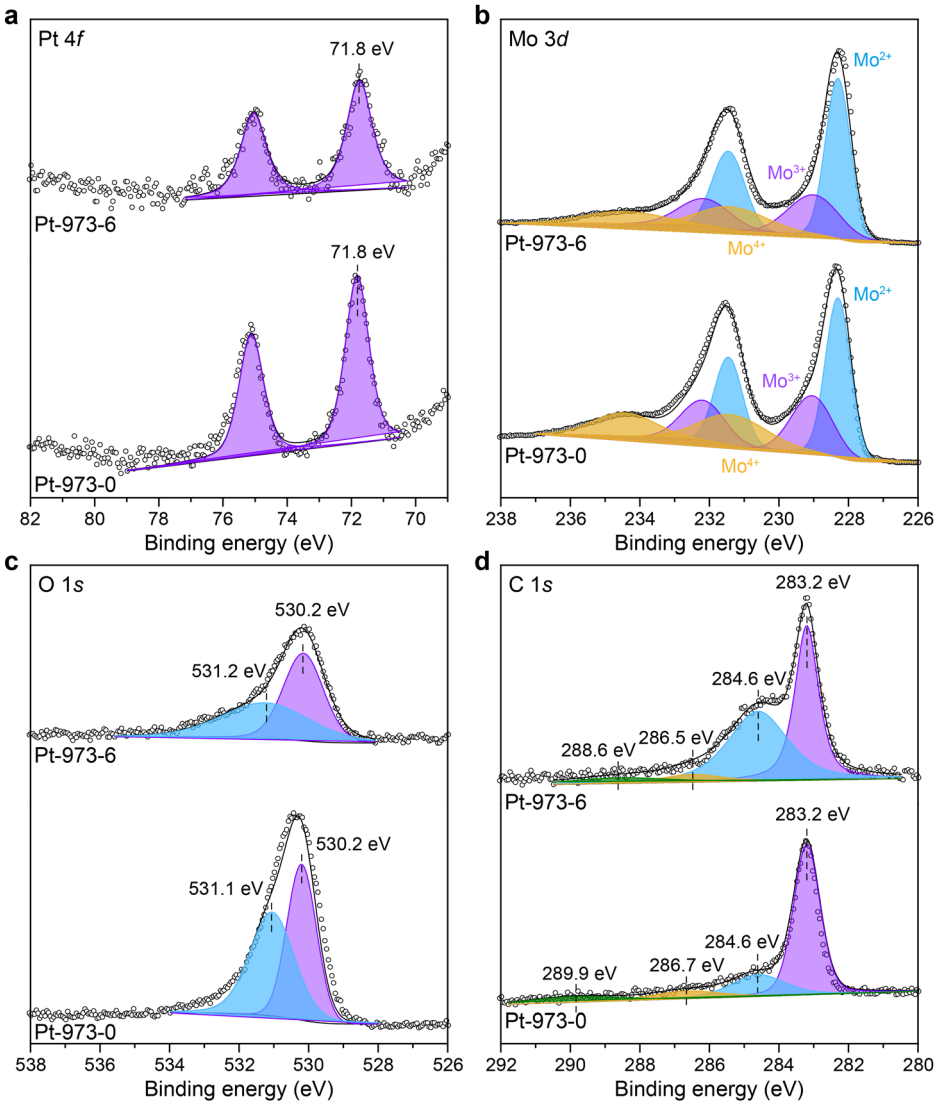

Fig. 7 XPS spectra of the Pt-973-*x* samples. (a) Pt 4f, (b) Mo 3d, (c) O 1s, (d) C 1s.

catalyst exhibited stable performance up to 100 hours at 393 K, during which the conversion of CO was around 24% at the early stage and slightly declined to 19% at the end of operation (Fig. S11, SI).

To reveal the structure change of the Pt-973-0 catalyst during the reaction, the spent catalyst after the WGS reaction for 2 hours was analyzed by STEM and XPS. STEM images verified that Pt still presented as bi/trilayers, along with a small proportion of single-atoms (Fig. S12, SI). XPS spectra suggested that the Pt thin layers basically remained in a metallic state, acting as the site for CO adsorption (Fig. S13, SI). The surface C/Mo ratio was practically identical before and after the reaction (0.43–0.44), while the surface-adsorbed hydroxyl groups were enriched. The ratio of adsorbed OH to lattice oxygen increased significantly from 1.09 in the fresh catalyst to 2.34 after the WGS reaction. This meant that MoC interacted with water under reaction conditions, generating reactive –OH species.

H_2O-IR experiments verified the superior ability of the Pt-973-0 catalyst for dissociating H_2O. When exposing the catalyst to water at 303 K, IR bands related to H_2O adsorption and dissociation appeared at 3100–3700 cm^{-1} (Fig. 11). In addition to the broad H_2O-related absorption band at 3413 cm^{-1} and –OH stretching band at 3178 cm^{-1}, the distinct bands at 3471 and 3234 cm^{-1} referred to reactive –OH species.[45–48] More importantly, the band at 3548 cm^{-1} might be attributed to PtOH species,[49] indicating that the –OH groups migrated from MoC to Pt. As the temperature was increased from 303 to 473 K, the H_2O-related band weakened significantly, while those for reactive –OH groups declined only moderately. At 393–473 K, the catalyst surface was dominated by reactive –OH species, demonstrating that the MoC support dissociated water efficiently. The possible migration of the dissociated –OH species to the Pt surface would be crucial for its reaction with CO, thereby serving as a determining factor for the high WGS activity. Most likely, Pt thin layers facilitated the adsorption of

© 2026 The Author(s). Published by the Royal Society of Chemistry

Open Access Article. Published on 15 September 2025. Downloaded on 2/8/2026 1:21:08 AM.
This article is licensed under a Creative Commons Attribution 3.0 Unported Licence.

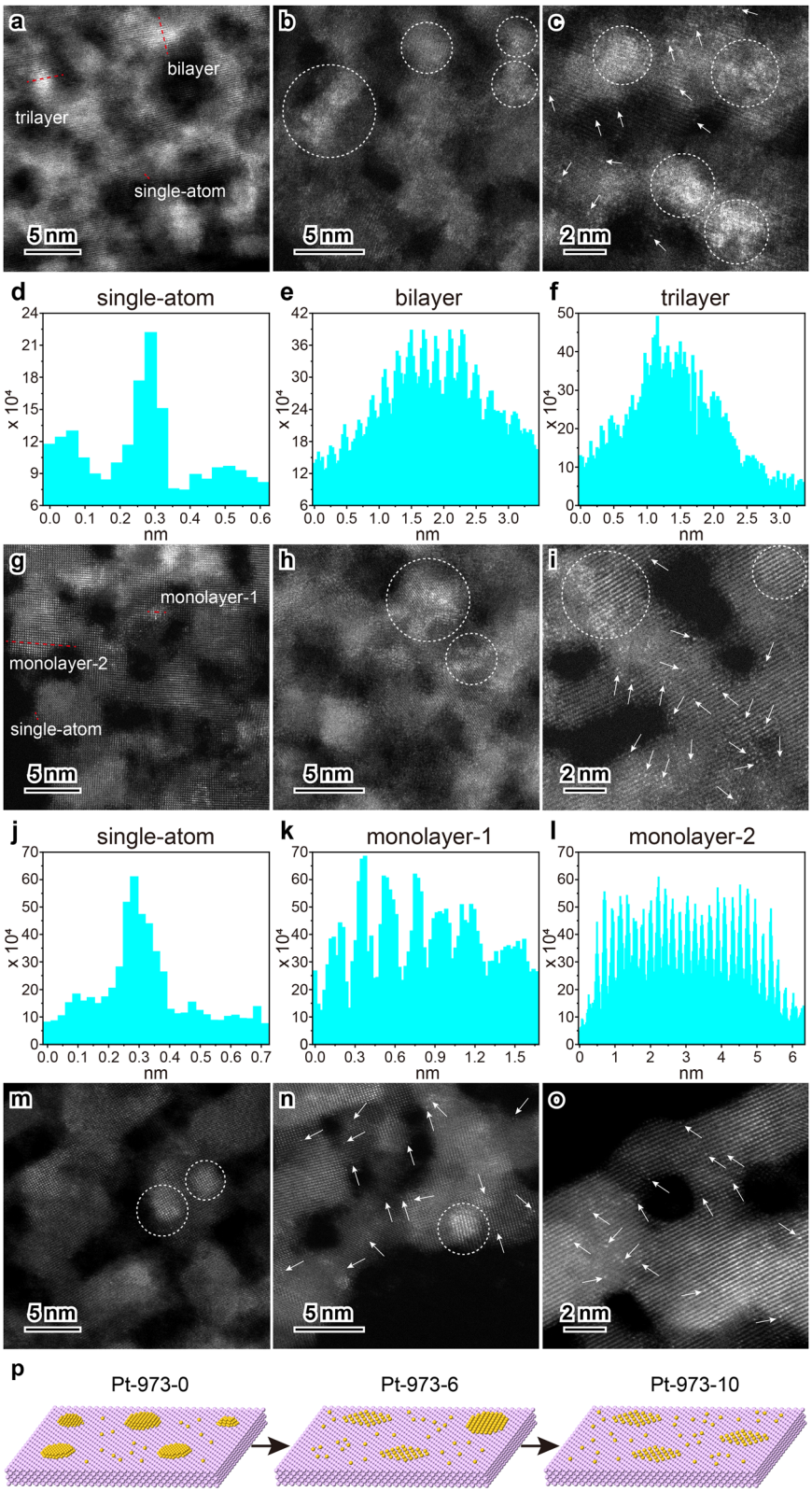

Fig. 8 Geometric structures of the Pt-973-0 (a)–(f), Pt-973-6 (g)–(l) and Pt-973-10 (m)–(o) samples. Pt thin layers are identified by comparing their line-scanning intensity profiles to those of neighboring Pt single-atoms. (p) A schematic illustration of redispersion of Pt thin layers to single-atoms/monolayers. The circles indicate Pt thin layers, while the arrows indicate Pt single-atoms.

© 2026 The Author(s). Published by the Royal Society of Chemistry

Open Access Article. Published on 15 September 2025. Downloaded on 2/8/2026 1:21:08 AM.
This article is licensed under a Creative Commons Attribution 3.0 Unported Licence.

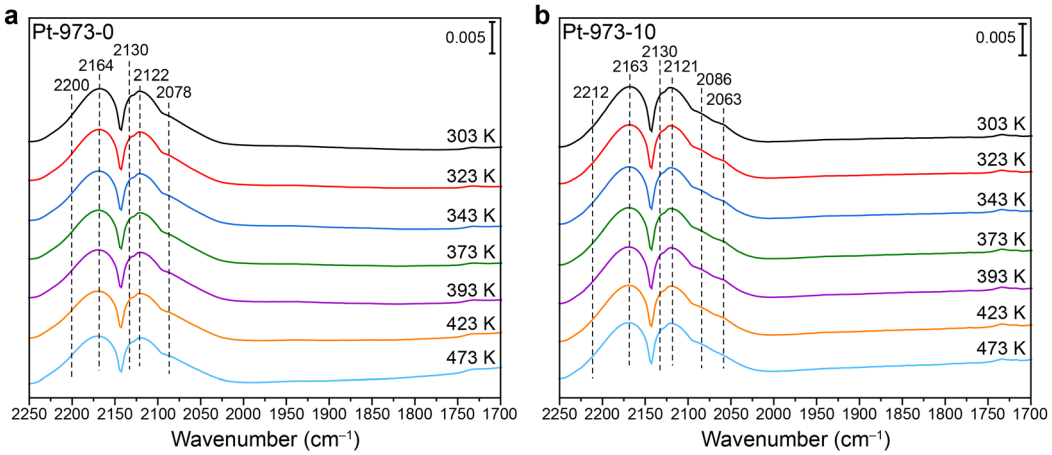

Fig. 9 IR spectra of CO adsorption on the Pt-973-0 (a) and Pt-973-10 (b) samples. The spectra were recorded under vacuum (1.0×10^{-5} mbar) at the specific temperatures.

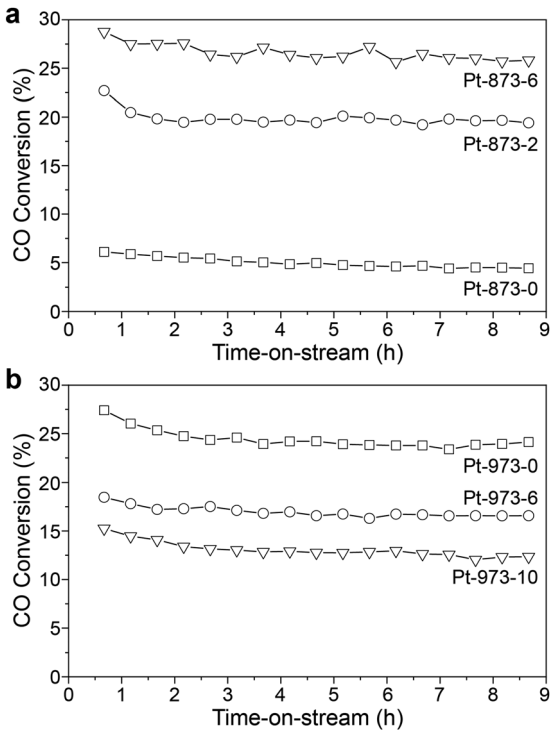

Fig. 10 Low-temperature WGS reaction over the Pt-873-*x* (a) and Pt-973-*x* (b) catalysts. Reaction conditions: 393 K, 3.0 vol% CO/6.0 vol% H_2O/He, and 50 000 mL g^{-1} h^{-1}. H_2 and CO_2 are detected as the only products without other by-products under the current reaction conditions.

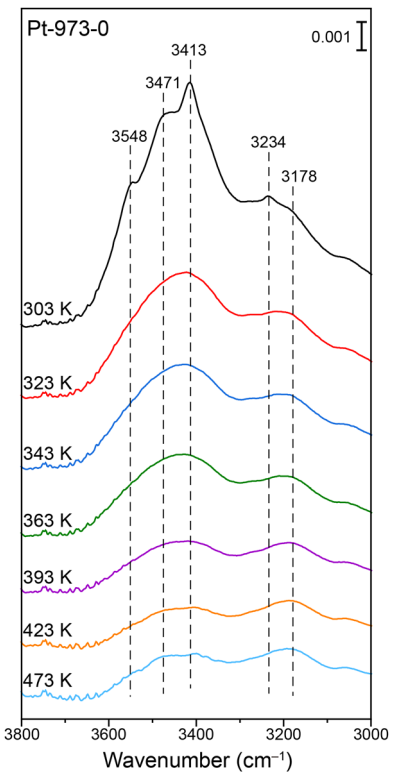

Fig. 11 IR spectra of H_2O adsorption on the Pt-973-0 catalyst. The spectra were recorded under vacuum (1.0×10^{-5} mbar) at the specific temperatures.

CO while MoC dissociated H_2O into reactive –OH species that migrated to the Pt surface and reacted with CO. This synergistic interaction resulted in the high WGS activity.

Conclusions

Carburization of a Pt/MoO_3 sample with a CH_4/H_2 mixture at 873–973 K could finely tune Pt dispersion over MoC. As MoO_3 underwent a topological transformation to α-MoC, the 3 nm Pt particles were progressively redispersed into thin layers and single-atoms. At 873 K, the Pt particles first collapsed and wetted the underlying MoC, then diffused on the MoC surface, and eventually redispersed to thin layers, mostly bilayers and trilayers. At a higher temperature, 973 K, the Pt thin layers were further dispersed into monolayers/single-atoms, along with the slightly enhanced crystallinity of α-MoC. The low-temperature

© 2026 The Author(s). Published by the Royal Society of Chemistry

Open Access Article. Published on 15 September 2025. Downloaded on 2/8/2026 1:21:08 AM. This article is licensed under a Creative Commons Attribution 3.0 Unported Licence.

WGS activity was found to increase as the 3 nm Pt particles redispersed into thin layers, but it decreased as they further dispersed into monolayers and single-atoms. This demonstrated that Pt bilayers and trilayers over MoC acted as the intrinsically more active species for the low-temperature WGS reaction that occurred at the Pt–MoC interface. Pt thin layers adsorbed and activated the CO molecule while the MoC support dissociated water into reactive –OH species that reacted with CO nearby. This synergistic interaction resulted in the high WGS activity, probably involving the migration of the dissociated –OH species on MoC to the Pt surface.

Author contributions

Peiyao Guo: catalyst synthesis, characterization, data analysis and manuscript writing; Yinghong Huang: characterization; Chuanchuan Jin: synthesis of molybdenum carbide; Di Zhou: synthesis of Pt particles; Shaobo Han: STEM analysis; Yan Zhou: conceptualization, result analysis, methodology, manuscript review and editing; Fan Yang: characterization; Wenjie Shen: conceptualization, result analysis, methodology, manuscript review and editing.

Conflicts of interest

There are no conflicts to declare.

Data availability

The data supporting this article have been included as part of the SI. Supplementary information: STEM images, WGS activity and stability, STEM images and XPS data after WGS reaction, and WGS activities of MoC-supported metal catalysts reported in the literature. See DOI: **https://doi.org/10.1039/d5ey00243e**.

Acknowledgements

This work was financially supported by the National Key R&D Program of China (2022YFA1604103) and the National Natural Science Foundation of China (22172168).

References

1 C. Ratnasamy and J. P. Wagner, *Catal. Rev.*, 2009, **51**, 325–440.
2 T. L. LeValley, A. R. Richard and M. Fan, *Int. J. Hydrogen Energy*, 2014, **39**, 16983–17000.
3 C. Rhodes, G. J. Hutchings and A. M. Ward, *Catal. Today*, 1995, **23**, 43–58.
4 K. D. Sabnis, M. C. Akatay, Y. Cui, F. G. Sollberger, E. A. Stach, J. T. Miller, W. N. Delgass and F. H. Ribeiro, *J. Catal.*, 2015, **330**, 442–451.
5 K. D. Sabnis, Y. Cui, M. C. Akatay, M. Shekhar, W.-S. Lee, J. T. Miller, W. N. Delgass and F. H. Ribeiro, *J. Catal.*, 2015, **331**, 162–171.
6 S. Tan, L. Wang, S. Saha, R. R. Fushimi and D. Li, *ACS Appl. Mater. Interfaces*, 2017, **9**, 9815–9822.
7 S. Yao, X. Zhang, W. Zhou, R. Gao, W. Xu, Y. Ye, L. Lin, X. Wen, P. Liu, B. Chen, E. Crumlin, J. Guo, Z. Zuo, W. Li, J. Xie, L. Lu, C. J. Kiely, L. Gu, C. Shi, J. A. Rodriguez and D. Ma, *Science*, 2017, **357**, 389–393.
8 J. Dong, Q. Fu, Z. Jiang, B. Mei and X. Bao, *J. Am. Chem. Soc.*, 2018, **140**, 13808–13816.
9 X. Zhang, M. Zhang, Y. Deng, M. Xu, L. Artiglia, W. Wen, R. Gao, B. Chen, S. Yao, X. Zhang, M. Peng, J. Yan, A. Li, Z. Jiang, X. Gao, S. Cao, C. Yang, A. J. Kropf, J. Shi, J. Xie, M. Bi, J. A. van Bokhoven, Y.-W. Li, X. Wen, M. Flytzani-Stephanopoulos, C. Shi, W. Zhou and D. Ma, *Nature*, 2021, **589**, 396–401.
10 L. Sun, J. Xu, X. Liu, B. Qiao, L. Li, Y. Ren, Q. Wan, J. Lin, S. Lin, X. Wang, H. Guo and T. Zhang, *ACS Catal.*, 2021, **11**, 5942–5950.
11 C. Jin, B. Wang, Y. Zhou, F. Yang, S. Han, P. Guo, Z. Liu and W. Shen, *ACS Catal.*, 2022, **12**, 15648–15657.
12 P. Guo, C. Jin, S. Han, Y. Zhou and W. Shen, *Catal. Sci. Technol.*, 2024, **14**, 4542–4549.
13 N. M. Schweitzer, J. A. Schaidle, O. K. Ezekoye, X. Pan, S. Linic and L. T. Thompson, *J. Am. Chem. Soc.*, 2011, **133**, 2378–2381.
14 X. Sun, J. Yu, S. Cao, A. Zimina, B. B. Sarma, J.-D. Grunwaldt, H. Xu, S. Li, Y. Liu and J. Sun, *J. Am. Chem. Soc.*, 2022, **144**, 22589–22598.
15 L. Lin, W. Zhou, R. Gao, S. Yao, X. Zhang, W. Xu, S. Zheng, Z. Jiang, Q. Yu, Y.-W. Li, C. Shi, X.-D. Wen and D. Ma, *Nature*, 2017, **544**, 80–83.
16 J. Li, L. Sun, Q. Wan, J. Lin, S. Lin and X. Wang, *J. Phys. Chem. Lett.*, 2021, **12**, 11415–11421.
17 R. Huang, M. Xia, Y. Zhang, C. Guan, Y. Wei, Z. Jiang, M. Li, B. Zhao, X. Hou, Y. Wei, Q. Chen, J. Hu, X. Cui, L. Yu and D. Deng, *Nat. Catal.*, 2023, **6**, 1005–1015.
18 T. Shao, L. Cao, L. Li, Y. Su, B. Hou, J. Lin and X. Wang, *Chem. Eng. J.*, 2024, **485**, 149967.
19 H. H. Hwu and J. G. Chen, *Chem. Rev.*, 2005, **105**, 185–212.
20 R. Li, J. Shang, F. Wang, Q. Lu, H. Yan, Y. Tuo, Y. Liu, X. Feng, X. Chen, D. Chen and C. Yang, *Nat. Commun.*, 2025, **16**, 1098.
21 Z. Li, Y. Li, E. Zhan, N. Ta and W. Shen, *J. Mater. Chem. A*, 2013, **1**, 15370–15376.
22 C. Jin, B. Wang, Y. Zhou, F. Yang, P. Guo, Z. Liu and W. Shen, *Chem. Commun.*, 2022, **58**, 7313–7316.
23 D. Zhou, S. Han, Y. Li, N. Ta, Y. Zhou, M. Li, S. Miao and W. Shen, *CrystEngComm*, 2021, **23**, 2447–2454.
24 Y. Cao, J. Luo, W. Huang, Y. Ling, J. Zhu, W.-X. Li, F. Yang and X. Bao, *J. Chem. Phys.*, 2020, **152**, 074714.
25 P. Delporte, F. Meunier, C. Pham-Huu, P. Vennegues, M. J. Ledoux and J. Guille, *Catal. Today*, 1995, **23**, 251–267.
26 J. S. Lee, L. Volpe, F. H. Ribeiro and M. Boudart, *J. Catal.*, 1988, **112**, 44–53.
27 Q. Fu, H. Saltsburg and M. Flytzani-Stephanopoulos, *Science*, 2003, **301**, 935–938.
28 X. I. Pereira-Hernández, A. DeLaRiva, V. Muravev, D. Kunwar, H. Xiong, B. Sudduth, M. Engelhard, L. Kovarik,

Open Access Article. Published on 15 September 2025. Downloaded on 2/8/2026 1:21:08 AM.
This article is licensed under a Creative Commons Attribution 3.0 Unported Licence.

E. J. M. Hensen, Y. Wang and A. K. Datye, *Nat. Commun.*, 2019, **10**, 1358.
29 F. Cai, J. J. Ibrahim, Y. Fu, W. Kong, J. Zhang and Y. Sun, *Appl. Catal., B*, 2020, **264**, 118500.
30 M. Peng, Y. Ge, R. Gao, J. Yang, A. Li, Z. Xie, Q. Yu, J. Zhang, H. Asakura, H. Zhang, Z. Liu, Q. Zhang, J. Deng, J. Zhou, W. Zhou, G. J. Hutchings and D. Ma, *Science*, 2025, **387**, 769–775.
31 R. Li, X. Zheng, F. Wang, H. Yan, X. Zhou, Y. Tuo, Y. Liu, X. Feng, X. Chen, D. Chen and C. Yang, *Chem. Eng. J.*, 2023, **474**, 145645.
32 K. Oshikawa, M. Nagai and S. Omi, *J. Phys. Chem. B*, 2001, **105**, 9124–9131.
33 J. Zhu, E. A. Uslamin, N. Kosinov and E. J. M. Hensen, *Catal. Sci. Technol.*, 2020, **10**, 3635–3645.
34 C. Zhao, C. Wang, H. Xin, H. Li, R. Li, B. Wang, W. Wei, Y. Cui and Q. Fu, *ACS Appl. Mater. Interfaces*, 2022, **14**, 26194–26203.
35 J. Raskó, *J. Catal.*, 2003, **217**, 478–486.
36 K. Ding, A. Gulec, A. M. Johnson, N. M. Schweitzer, G. D. Stucky, L. D. Marks and P. C. Stair, *Science*, 2015, **350**, 189–192.
37 L. DeRita, S. Dai, K. Lopez-Zepeda, N. Pham, G. W. Graham, X. Pan and P. Christopher, *J. Am. Chem. Soc.*, 2017, **139**, 14150–14165.
38 A. Liu, X. Liu, L. Liu, Y. Pu, K. Guo, W. Tan, S. Gao, Y. Luo, S. Yu, R. Si, B. Shan, F. Gao and L. Dong, *ACS Catal.*, 2019, **9**, 7759–7768.
39 W. Zhao, J. Wang, X. Zhang, G. Zhang, Y. Li, Z. Jiang, M. Li, Y. Zhou, Y. Wang and W. Shen, *ACS Catal.*, 2024, **14**, 13591–13601.
40 W. Wu, Z. Wu, C. Liang, X. Chen, P. Ying and C. Li, *J. Phys. Chem. B*, 2003, **107**, 7088–7094.
41 W. Wu, Z. Wu, C. Liang, P. Ying, Z. Feng and C. Li, *Phys. Chem. Chem. Phys.*, 2004, **6**, 5603–5608.
42 A. Susarrey-Arce, R. M. Tiggelaar, J. G. E. Gardeniers, A. van Houselt and L. Lefferts, *J. Phys. Chem. C*, 2015, **119**, 24887–24894.
43 J. Li, Q. Guan, H. Wu, W. Liu, Y. Lin, Z. Sun, X. Ye, X. Zheng, H. Pan, J. Zhu, S. Chen, W. Zhang, S. Wei and J. Lu, *J. Am. Chem. Soc.*, 2019, **141**, 14515–14519.
44 Z. Zhang, J. Tian, Y. Lu, S. Yang, D. Jiang, W. Huang, Y. Li, J. Hong, A. S. Hoffman, S. R. Bare, M. H. Engelhard, A. K. Datye and Y. Wang, *Nat. Commun.*, 2023, **14**, 2664.
45 N. B. Colthup, L. H. Daly and S. E. Wiberley, in *Introduction to Infrared and Raman Spectroscopy*, ed. N. B. Colthup, L. H. Daly and S. E. Wiberley, Academic Press, San Diego, 3rd edn, 1990, pp. 387–481.
46 K. S. Finnie, D. J. Cassidy, J. R. Bartlett and J. L. Woolfrey, *Langmuir*, 2001, **17**, 816–820.
47 F. Dai, Q. Zhuang, G. Huang, H. Deng and X. Zhang, *ACS Omega*, 2023, **8**, 17064–17076.
48 N. Tang, D. Liu, S. Chen, Z. Wang, Y. Ma, Q. Li, Y. Li, G. Xu, C. Wu, L. Kang, W. Luo, B. Qiao, H. Zhu and Y. Cong, *ACS Catal.*, 2024, **14**, 14297–14307.
49 B. A. Morrow and P. Ramamurthy, *Can. J. Chem.*, 1971, **49**, 3409–3410.

© 2026 The Author(s). Published by the Royal Society of Chemistry